$L1_0$-FeNi ordered phase in AC electrodeposited iron-nickel biphasic nanowires

Fernando Meneses[1,2], Analía Pedernera[1,2], Cecilia Blanco[1], Noelia Bajales[1,2], Silvia E. Urreta[1], Paula G. Bercoff[1,2]*

1. FAMAF, Universidad Nacional de Córdoba. Medina Allende s/n. Ciudad Universitaria, X5000HUA, Córdoba, Argentina.
2. IFEG, CONICET. Medina Allende s/n. Ciudad Universitaria, X5000HUA, Córdoba, Argentina.

Keywords: Fe-Ni polycrystalline nanowires; AC electrodeposition; magnetization mechanisms; $L1_0$ FeNi phase

* Author to whom correspondence should be addressed: bercoff@famaf.unc.edu.ar

Abstract

Nanowire arrays with nominal composition Fe_xNi_{100-x} (x = 0, 18, 53, 93, 100) have been synthesized by AC electrodeposition into the cylindrical pores of alumina templates. Except for the composition $Fe_{53}Ni_{47}$, nanowires are single-phase, consisting of small grains of the A1-FeNi disordered phase. Near the equiatomic nominal composition nanowires are biphasic, consisting of grains of the A1-FeNi disordered phase (γ-FeNi phase) as well as grains of the $L1_0$-FeNi ordered phase (γ''-FeNi phase). Even in nanowires with high Fe content the α-Fe *bcc* phase is absent. The coercive field and reduced remanence dependences on composition are non monotonic but go through a local maximum near the equiatomic composition. Biphasic nanowires behave as a magnetic single phase, exhibiting a unique switching field for polarization reversal in the entire range between 5 K and 300 K. The linear dependence of the coercive field on temperature and the dependence of the coercive field on the angle between the nanowire long axis and the applied field are consistent with a polarization reversal mechanism controlled by the nucleation by curling and expansion of inverse domains, assisted by thermal fluctuations and the applied field. The effective uniaxial anisotropy resulting from these measurements suggests that the shape anisotropy makes a small contribution to the high coercive field observed (170 mT). The effective uniaxial magnetocrystalline constant measured at room temperature, 130 - 170 k Jm^{-3}, may be explained by considering nucleation at favorable sites in an exchange-hardened γ-FeNi soft phase.

1. Introduction

Fe-Ni phases compose the Earth's core, iron meteorites and steels. Ni stabilizes the γ-iron phase leading to extensively used austenitic steels. Three Fe-Ni compositions of technical interest are found in magnetic iron-nickel bulk alloys, generically named permalloys [1]. Near the composition 22 at.% iron, magnetostriction and magnetocrystalline anisotropy both pass through zero leading to a high initial permeability. The 35 at.% iron permalloys show a strong response to field annealing while maintaining the magnetic anisotropy constant $K \approx 0$, and 50 at.% iron permalloy is important because of its high flux density of about 1.6 T and the field annealing capability, leading to very square hysteresis loops. These special properties are in principle expected in Fe-Ni nanostructures but modified to different extents by the surface, shape and confinement effects.

Among magnetic nanostructures, one-dimensional bimetallic ones have been extensively explored in recent years because of their new properties arising from surface and small size effects. Ferromagnetic nanowires (NWs) are of special interest because of their large shape anisotropy, especially useful in applications such as high-frequency devices and domain-wall based logic and memory devices [2, 3]. When compared to traditional high-frequency ferrites, ferromagnetic metallic nanowires have higher saturation magnetization and a larger shape anisotropy, which can provide higher permeability. The magnetic anisotropy of a ferromagnetic nanowire can be adjusted by controlling the crystal structure [4], composition [5] and the intrinsic exchange coupling [6].

It is nowadays accepted that most of the physical properties of bulk Fe-Ni alloys are conditioned by the coexistence and significant interplay of spatial atomic configuration and magnetic moment orders, [7] being composition and coexisting phases the key parameters [8]. In the case of NWs, additional variables such as diameter, length and grain size [9] must be also considered.

The accepted version of the Fe-Ni phase diagram contains a γ-phase field extending at high temperatures from pure *fcc*-Fe to pure *fcc*-Ni. At lower temperatures, terminal solid solutions based on the *bcc* α and δ phases of iron, and a stable intermetallic compound γ'-Ni_3Fe with the $L1_2$ structure are expected [10]. In meteorite specimens, a γ''-FeNi phase with the $L1_0$ structure has also been found [11]. The precipitation of this latter phase is only possible under extremely slow (millions of years) cooling conditions that are realized in meteorite alloys but inaccessible under laboratory conditions. Nevertheless, it is accepted that the stable phases below ~400 °C in the low Ni region of the Fe-Ni phase diagram are *bcc*-α with 4 wt. % Ni and A1-FeNi with 51.4 wt. % Ni. Below ~320 °C, the A1-FeNi phase orders to form γ'' with the $L1_0$ structure [12].

Electrodeposition of Fe-Ni NWs into porous alumina templates is relatively simple and a low cost processing route, easily scalable to industrial production [13]. Ordered nanowire Fe-Ni arrays have been extensively synthesized by DC and pulsed current techniques as reported in many works [9, 14, 15].

On the contrary, AC electrodeposition of Fe-Ni NWs into narrow alumina pores is less frequent, and the description of microstructure, phases and magnetic properties of different resulting nanostructures is not complete. The AC electrodeposition takes place far from equilibrium, promoting metastable phases. Then, it is worth to explore in which phase/phases NWs electrocrystallize for different processing variables, and the resulting compositions.

The aim of our work was to obtain small grained, granular nanowires suitable for applications where large surface-to-volume rates are necessary, such as catalysis, electro catalysis or sensing. These granular wires exhibit irregular surfaces with areas which are chemically and crystallographically different, also with distinct properties, and many grain boundaries intersections with the external surface, providing diffusion short-circuits, ideal for the incorporation of atoms from the surroundings.

In this work, Fe-Ni NWs with different compositions are synthesized by AC electrodeposition into the cylindrical pores of an alumina template. Morphology, composition and the resulting phases after the electrocrystallization inside the relatively thin template pores (~20 nm) are determined. Also, magnetic hysteresis properties such as coercivity, reduced remanence and the mechanism for magnetization reversal under an applied field are determined and correlated with composition and the electrocrystallized phases. From a basic point of view, hysteresis properties and magnetization reversal processes and mechanisms in granular nanowires are somewhat different from those found in single-crystalline and large-grained cylindrical nanowires.

It is found that near the equiatomic nominal composition the arrays exhibit interesting features. NWs consist of grains of A1-FeNi (γ-FeNi disordered phase) coexisting with $L1_0$-FeNi (γ''-FeNi ordered phase) grains. Exchange coupling between these grains lead to a harder, single magnetic phase behavior.

2. Experimental procedures

Fe_xNi_{100-x} (x = 0, 18, 53, 93, 100) NWs are synthesized by AC electrodeposition into the pores of alumina templates (AAO) obtained by the conventional two-step anodization process [13] performed on high-purity aluminum foils (99.995%). Previous to anodization, aluminum foils are first degreased with acetone, then electro-polished in a H_2SO_4 + H_3PO_4 + H_2O 2:2:1 solution, and finally etched with NaOH to remove surface oxides. The first anodization is performed under a constant voltage of 20 V in 0.3 M $(COOH)_2$ for 4 h at 2 °C to grow a layer of porous alumina. Even when the use of (COOH)2 (oxalic acid) for Al anodization is usually combined with a voltage of 40 V for obtaining well-ordered and smooth pores of ~40 nm in diameter, in this work a lower voltage is purposedly used to increase the pores' rugosity. The aluminum oxide film is then dissolved in 0.2 M Cr_2O_3 and 0.4 M H_3PO_4 at 60 °C for 1 h. A second anodizing step is performed applying the same conditions as in the first one, but for 2 h. The insulating layer resulting at the pore bottom (barrier layer) must be overcome by the ions in the electrolytic bath. Even when for pore diameters near 20 nm and the high potential applied the conduction across this barrier is possible [16, 17], in order to improve conduction this barrier layer is thinned by immersion in a diluted solution of H_3PO_4 5% v/v only for a few minutes, so that the pores' diameters are not too widened. Figure 1.a shows the resulting template, with ordered pores ~20 nm in diameter and about 3-4 μm in length. The template porosity P $(= (\pi/2\sqrt{3})(D_p/D_{int})^2)$ is (0.10 ± 0.01) [18], according to the measured values of the mean pore diameter $D_p = (20 \pm 2)$ nm and the mean centre-to-centre inter-pore distance in the array, $D_{int} = (60 \pm 4)\text{nm}$.

For the synthesis of NWs, an electrochemical cell operating with two-electrodes is used, in which the remaining aluminum support of the anodized film serves as a working electrode, and a graphite rod as an auxiliary one. Before each deposition, oxygen is purged from the solution by intense nitrogen bubbling.

Pure Fe NWs are electrodeposited from an aqueous electrolytic solution prepared with 0.2 M $FeSO_4 \cdot 7H_2O$, 4.5 mM ascorbic acid (to avoid iron oxidation) and 0.5 M H_3BO_3 to enhance conductivity. The pH value, controlled by adding few drops of diluted H_2SO_4, is adjusted to 5. Fe_xNi_{100-x} NWs are prepared using $NiSO_4 \cdot 6H_2O$ mixed in different proportions with $FeSO_4 \cdot 7H_2O$ (detailed in Table 1). Electrodepositions are conducted under a sinusoidal wave of 200 Hz and 16 V_{rms}, for 2 min, at room temperature.

Samples are denominated FeX, with X the iron atomic percent and Ni100 in the case of pure Ni NWs.

Table 1. Composition of the electrolytes used for the electrodeposition of the different samples.

Sample	$NiSO_4 \cdot 6H_2O$ [g/l]	$FeSO_4 \cdot 7H_2O$ [g/l]	H_3BO_3 [g/l]	$C_6H_8O_6$ [g/l]
Ni100	60	-	30	-
Fe18	90	6	30	0.75
Fe53	90	12	30	0.75
Fe93	50	50	30	0.75
Fe100	-	30	30	0.75

Crystallographic phases in the nanowires are identified by X-ray diffraction (XRD); the measured profiles are recorded in a Panalytical X'PertPro diffractometer (40 kV, 40 mA), in Bragg–Brentano reflection geometry using Cu Kα radiation (λ= 1.5418 Å), in the 2θ range from 30° to 90 °. The cell parameters are refined with the Rietveld method using the FULLPROF software. A pseudo-Voigt shape function is always adequate to obtain good fits for experimental data. Corresponding crystallite sizes, given by the Scherrer equation, are also estimated.

The mean composition of each array is determined by energy-dispersive X-ray spectroscopy (EDS), in an Oxford Energy Dispersive Spectrometer equipment, and the nanowire morphology investigated in a scanning electron microscope (FE-SEM) Zeiss. Samples are investigated by SEM after dissolving the template in a 1.0 M NaOH solution to separate the NWs. Dispersed nanowires are obtained for each composition after sonication and rinsing in distilled water.

Room temperature magnetic properties of Fe_xNi_{100-x} NWs are measured in a vibrating sample magnetometer (VSM) Lakeshore 7300, with magnetic fields up to 1.3 T, a large-enough value to saturate all the samples. A commercial Magnetic Property Measurement System (MPMS Quantum Design) is used to explore the temperature dependence of the magnetic properties between 5 K and 300 K.

Two orientations of the external field are considered for the magnetic measurements: parallel (PA) and perpendicular (PE) to the NWs long axis. The total magnetic moment of the array is assumed to be the simple superposition of contributions from the metallic wires filling the pores (ferromagnetic), the alumina template (diamagnetic) and the Al support (paramagnetic), so the ferromagnetic component in each loop is estimated after subtracting a linear contribution.

3. Results and Discussion

3.1. Morphology and structure

Nanowires of three different nominal compositions, exhibiting irregular morphologies and rough surfaces, are shown in Figures 1.b to 1.d. Surface conditions and branching are found in FeNi nanowires mainly due to the electrocrystallization process, controlled by Fe and Ni diffusion in the electrolyte and their incorporation at the interface of the growing crystal. Nanowires' morphologies strongly depend on the electrocrystallization process controlled by the solid phase nucleation, growth and diffusion of the metallic species near the interface. As previously indicated, the mean (nominal) composition of the arrays is determined by EDS, after dissolution of both, the remaining Al support and the alumina template. The mean values reported, $Fe_{18}Ni_{82}$ (Fe18), $Fe_{53}Ni_{47}$ (Fe53) and $Fe_{93}Ni_{07}$ (Fe93), correspond to the average of ten different regions in each sample. The mean NWs' length corresponding to the different compositions are listed in Table 2.

Table 2. Morphological and structural parameters for *fcc* Fe_xNi_{100-x} alloyed NWs of (20 ± 2) nm mean diameter *D*, length *L* and aspect ratio $A_r = L/D$. Phases detected, lattice constant a_0, and crystallite size d_{Sch}, estimated using the Scherrer equation, are also listed.

Sample	*L* [μm]	A_r	Phases	a_0 [Å]	d_{Sch} [nm]
Fe18	1.0 ± 0.1	50 ± 7	A1-FeNi	3.613(1)	20 ± 5
Fe53	0.8 ± 0.1	40 ± 6	$L1_0$-FeNi	3.586(1)	19 ± 5
			A1-FeNi	3.611(1)	22 ± 5
Fe93	0.6 ± 0.1	30 ± 6	A1-FeNi	3.601(1)	20 ± 5

Figure 2 shows the X-ray diffractograms corresponding to the as-prepared Ni, Fe and Fe-Ni NWs, still ordered inside the AAO template. The Al substrate was removed before measuring samples Fe100 and Ni100. Iron NWs have a *bcc* cubic structure (PDF # 00-006-0696), with a preferred (110) orientation along the wires' long axis. All samples containing Ni exhibit broad peaks at 43.71° and 50.8° which are indexed, respectively, as the (111) and (200) peaks of the A1-FeNi phase (tabulated in card PDF# 00-047-1405). The large peak at about 44.9° corresponds to aluminum substrate. The resulting lattice constant value a_0 of the Ni-containing phases in the nanowires are listed in Table 2.

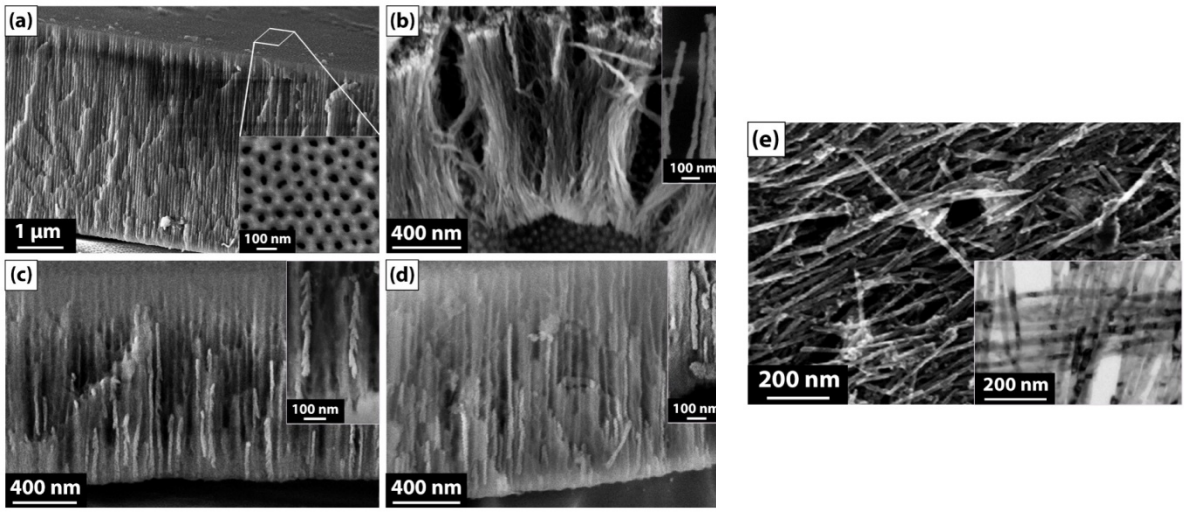

Figure 1. SEM images showing (a) side and top views of an alumina template of 20 nm mean pore diameter, and (b) $Fe_{18}Ni_{82}$; (c) $Fe_{53}Ni_{47}$; (d) $Fe_{93}Ni_{07}$ nanowires still embedded in the AAO templates. (e) SEM image of pure Fe nanowires, released from the template. The inset in (e) is a bright field TEM image of Fe nanowires, illustrating the large grain size and the surface condition.

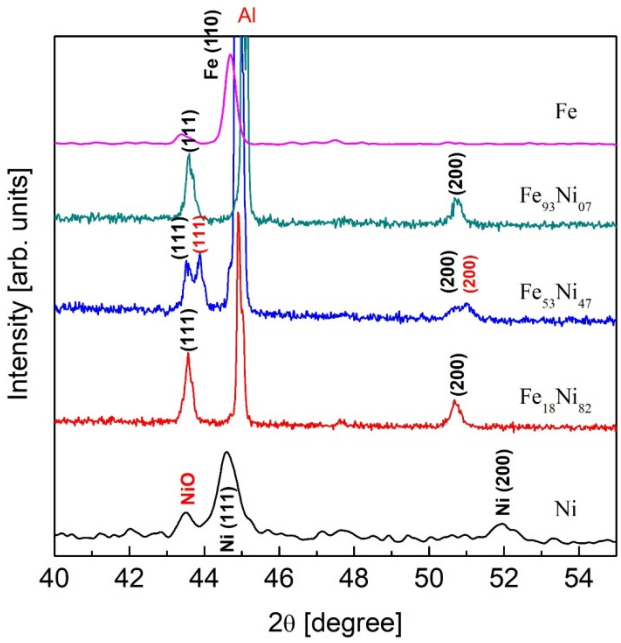

Figure 2. XRD diagrams corresponding to Ni, $Fe_{18}Ni_{82}$, $Fe_{53}Ni_{47}$ and $Fe_{93}Ni_{07}$ and Fe NWs arrays. The FeNi (111) and (200) reflections corresponding to phase $L1_0$ are clearly resolved in the spectrum of sample Fe53 and are indexed in red, to the right of the A1-FeNi peaks.

It may be observed that peaks corresponding to α-Fe reflections are absent, even in sample Fe93. This is in contradiction with results previously reported by M. Almasi Kashi *et al.* [8], where AC electrodeposited Fe_xNi_{100-x} NWs containing more than 70 at.% Fe were found to have a *bcc* structure. At present, we are unable to explain this difference as well as other dissimilarities found in the resulting microstructures, such as the appearance of an ordered FeNi phase near the equiatomic composition, which has not been reported by other authors for AC electrodeposited FeNi structures. Peaks arising from the *fcc*-FeNi phase are broad, indicating that NWs are granular, with small crystallite size (~20 nm). It may be also observed in the diffractogram of sample Fe53 that all the peaks associated to the *fcc*-FeNi phase split in two clearly resolved components, indicating that two phases coexist in the NW array. As shown in Table 2, the lattice constants of these *fcc* phases differ in 0.7 % while no significant difference between their crystallite sizes is found. Considering the room temperature values of the lattice constant for nickel a_0 (Ni) = 3.524 Å [19] and for gamma iron a_0 (γFe) = 3.583 Å [20], the splitting observed in the diffraction peaks of Fe53 NWs cannot be explained assuming different compositions and the validity of Vegard's law in this binary system.

This fact strongly suggests that these two peaks are related to different atomic orderings. In this sense, Kotsugi *et al.* studied the $L1_0$-FeNi phase in samples extracted from a natural meteorite [21]. They compared the XRD pattern of this phase with that corresponding to an alloy with the same composition but disordered. After carrying out a Rietveld analysis of wide angle XRD patterns, the lattice parameters of $L1_0$-FeNi phase were estimated as $a = b = 3.582$ Å and $c = 3.607$ Å ($c/a = 1.007$), and those of disordered FeNi were $a = b = c = 3.603$ Å.

In sample Fe53, the two resolved peaks for reflections (111) and (200) observed in Figure 2 can be assigned to the disordered A1-FeNi phase (at smaller diffraction angles) and to the $L1_0$-FeNi ordered phase (to the right of the A1-FeNi phase peaks). For the other two compositions, NWs mainly consist of a Fe-Ni disordered phase.

3.2. *Room temperature magnetic properties*

The effect of Ni content on the microstructure and magnetic properties of FeNi nanowires are investigated. The considered microstructural variables are the grain size and the different phases that form during the electrocrystallization process. Magnetic and structural properties of pure Fe and Ni nanowires are only considered as references for large-grained, relatively smooth cylinders. The nanowires' morphology and surface irregularities are not quantitatively characterized to attempt a rigorous correlation with the observed magnetic properties, so the effect of these irregularities on the hysteresis properties of FeNi alloyed NWs are only discussed in quite general terms.

Figure 3 depicts the room-temperature hysteresis loops of all the samples in the as-synthesized condition (NWs embedded in the AAO templates), with the applied magnetic field parallel and perpendicular to the NWs long axis. In all the arrays, the easy magnetization axis is parallel to the NWs long axis, due to hysteresis mechanisms governed by shape anisotropy. The hysteresis loop of sample Fe53 shows no evidence of two uncoupled (A1-type disordered Fe-Ni and the ordered $L1_0$-FeNi) magnetic phases, as confirmed by a unique peak in the differential susceptibility shown in the top-left inset of Figure 3.c.

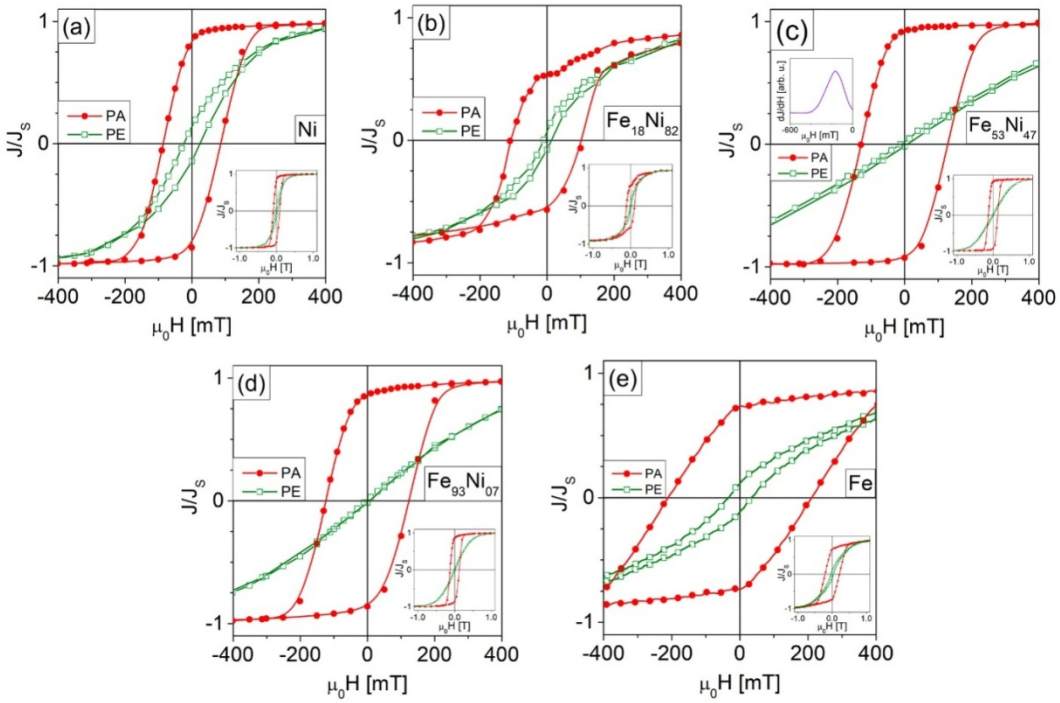

Figure3. Room temperature hysteresis loops of samples with different atomic compositions: (a) Ni, (b) $Fe_{18}Ni_{82}$, (c) $Fe_{53}Ni_{47}$, (d) $Fe_{93}Ni_{07}$ and (e) Fe. Measurements are performed with the applied field parallel (PA, full circles) and perpendicular (PE, open squares) to the NWs long axis. Right corner insets show the complete loops.

As shown in Figure 4.a, coercivity as a function of composition increases with iron content, goes through a small broad maximum near 53 at.% Fe and then drops for Fe93. When the small amount of Ni is removed (7 at.%), coercivity suddenly increases up to the pure Fe value. A similar trend may be guessed for coercivity in the PE configuration; however no rigorous conclusions may be stated because of large experimental uncertainties. This coercive field dependence on the Fe content is different to that reported by M. Almasi Kashi *et al.*, [8] who find that for Fe contents less than 50 at.% the coercivity slowly increases with the iron atomic fraction, but over 50 at.% Fe it increases at a higher rate reaching the maximum coercivity near $Fe_{93}Ni_{07}$ due to the large iron content.

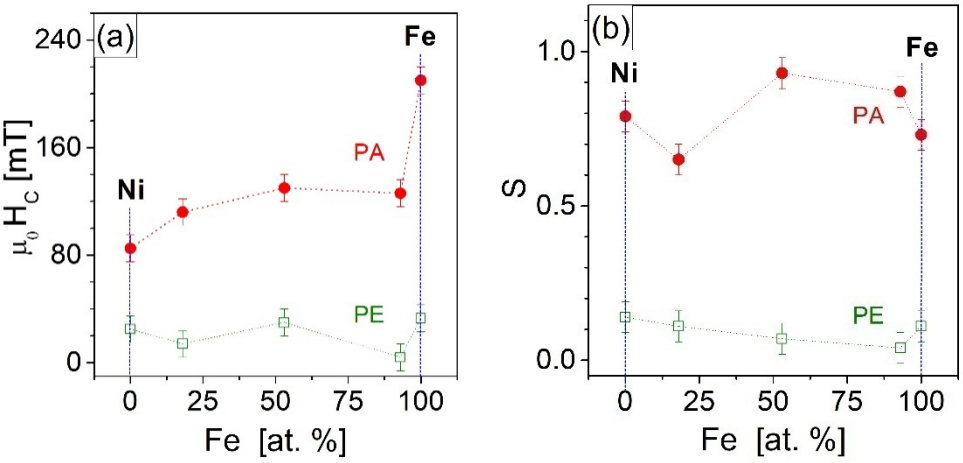

Figure 4. Dependence of the hysteresis properties on the NWs composition, in parallel (PA, full circles) and perpendicular (PE, open squares) configurations. (a) Coercive field and (b) relative remanence or squareness *S*.

Squareness, defined as the ratio of remanent polarization J_R and saturation polarization J_S ($S = J_R/J_S$), first slightly increases up to a Fe content of 53 at.%, corresponding to the two-phase nanowire array, decreasing then for smaller Fe content in PA configuration. Again, small coercivity values accompanied by large experimental errors prevent establishing a clear behavior for PE configuration. The parameters corresponding to each loop at 300 K are displayed as functions of composition in Figure 4 and listed in Table 3. These non-monotonic dependences of coercivity and squareness on composition found in the present work cannot be rationalized by considering coercivity controlled only by shape anisotropy, but by an effective anisotropy resulting from contributions of shape and magnetocrystalline anisotropies. Near the equiatomic composition, the presence of a given volume fraction of the $L1_0$-FeNi ordered phase coexisting with the disordered one, reduces shape anisotropy K_{sh} because of its lower saturation polarization (K_{sh} α J_s^2). However, this ordered phase contributes with a two-orders-of-magnitude larger crystalline anisotropy, compensating for this reduction and leading to the slightly larger coercive field value observed in this composition range, as reported by Kojima et al. [22]. These authors find that the composition ratio of natural (from meteorites) $L1_0$-FeNi is (50±2) at.% Fe; (49±2) at.% Ni, and confirm they exhibit a quite high coercivity, up to 120 mT in bulk.

Biphasic $Fe_{53}Ni_{47}$ NWs with almost equiatomic nominal composition exhibit interesting features: an enhanced coercivity and a clear single magnetic phase behavior. In what follows, aspects like the

temperature dependence of coercivity and squareness, and the magnetization reversal mechanism in arrays with this composition are further investigated.

Table 3. Coercive fields $\mu_0 H_C$(PA), $\mu_0 H_C$(PE) and squareness factors [$S=J_R/J_S$] S(PA) and S(PE), as determined with the applied field parallel (PA) and perpendicular (PE) to the NWs long axis, at 300 K. J_S and K_1 values are also reported [23].

Sample	$\mu_0 H_C$(PA) [mT]	$\mu_0 H_C$(PE) [mT]	S(PA)	S(PE)	J_S [T]	K_1 [kJ m^{-3}]
Fe100	210 ± 10	35 ± 10	0.73(5)	0.11(5)	2.15	+48
Fe93	125 ± 10	5 ± 10	0.87(5)	0.04(5)	-	-
Fe53	170 ± 10	40 ± 10	0.93(5)	0.07(5)	1.68 1.38†	+1.1 +700†
Fe18	110 ± 10	15 ± 10	0.65(5)	0.11(5)	1.04	-1.38
Ni100	85 ± 10	25 ± 10	0.79(5)	0.14(5)	0.62	-5.7

† $L1_0$ Phase from ref. [22]

3.3. *Magnetization mechanisms*

The magnetization reversal mechanism that takes place in a particular system may be determined if the magnetic polarization and the coercive field are known as functions of both the temperature and the angle between the magnetic field and the easy axis of the NWs (parallel to the long axis).

Figure 5.a depicts the temperature dependence of magnetization between 5K and 300 K, measured following the Zero Field Cooling-Field Cooling (ZFC-FC) protocol, under a magnetic field of 10 mT for PA orientation. As expected, the observed behavior is characteristic of ferromagnets, with an irreversibility temperature above 300 K. Small vertical arrows indicate local maxima in the relative polarization $J(T)/J(T=300K)$.

Figure 5.b shows the profile of the blocking temperature distribution [24], corresponding to the ZFC-FC curves in Figure 5.a for the PA configuration. Two maxima are identified, a narrow peak at about 30 K and a quite broad almost uniform distribution centered near 180 K. Assuming that magnetization reversal initiates by a localized, non-homogeneous nucleation mode, these maxima roughly indicate [25] the blocking temperature of the mechanism in each phase, that is, the temperature above which this thermally activated, field-assisted reversal mechanism operates. Below these temperatures the magnetization reversal mechanisms become inactive. The maximum at 180 K may be associated to nucleation at the magnetically harder $L1_0$-FeNi ordered phase while that at 30 K, to the softer A1-FeNi one.

Magnetocrystalline anisotropy constants of 1.1 kJ/m^3 (for A1-FeNi) and 700 kJ/m^3 (for $L1_0$-FeNi) have been reported for these phases [22, 26], leading to activation volumes V_{ac} = (20 $k_B T/K_1$), assumed as reversal nuclei, of (4.1 nm)^3 and (19 nm)^3 for blocking temperatures 180 K and 30 K, respectively. The activation volume obtained for the soft phase, practically an entire grain, seems somewhat large to be accessible to thermal activation, suggesting that the effective anisotropy value of this disordered phase is larger than the assumed one. The mean nucleus size in the hard phase is relatively close to exchange length parameter $l_w = (A/K)^{1/2}$ = 4.6 nm (being A = 1.5 x 10^{-11} J/m, the exchange energy constant and K the corresponding effective magnetocrystalline anisotropy). Scaling the nucleus size in the soft phase to the

relevant magnetic length l_{ex} = $(2A\ \mu_0/\ J_S^2)^{1/2}$ = 3.65 nm, an effective anisotropy of 170 kJ/m^3 results for the nucleation event in the soft phase.

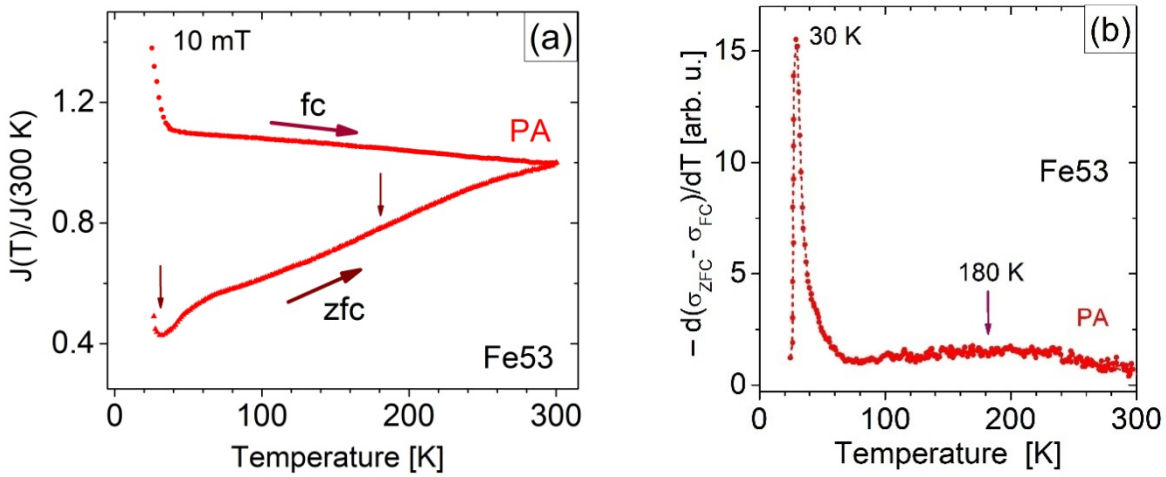

Figure 5. (a) Relative magnetization and (b) magnetization activation barrier distribution as functions of temperature in sample Fe53 (PA configuration). Properties were measured following the ZFC-FC protocols, under an applied field of 10 mT [24].

At room temperature, nucleation is completely active in both phases; however, no separate reversion events are detected in the hysteresis loop of Figure 3.c (see also a single peak in the differential susceptibility shown in the inset of this figure). This behavior is consistent with an efficient exchange-coupling between hard and soft grains, which may be the origin of the hardening observed in Figure 4 for compositions near the equiatomic one. In absence of the exchange hardening provided by the $L1_0$-FeNi phase, a monotonic increase of coercivity with iron content, arising from shape anisotropy is expected, as that reported by A. Kashi *et al.* [8].

The temperature dependence of the coercive field corresponding to the PA configuration is shown in Figure 6 for samples Fe53 and Fe100. This latter array, with NWs exhibiting the highest shape anisotropy (due to its high saturation polarization), relatively smooth surface and quite large (~100 nm) grain size, is shown for comparison. The coercive field in Fe53 and Fe100 arrays gradually increases (42% in Fe53 and 39% in Fe100 NWs) when temperature decreases from 300 K to 5 K.

Assuming a thermally-activated reversal mechanism, controlled by nucleation of inverse domains, the activation energy barrier E and the coercive field $\mu_0 H_C$ are related. For an applied field H, the energy barrier height is given by [27]:

$$E = E_0 \left(1 - \frac{H}{H_0}\right), \tag{1}$$

where E_0 is the activation energy barrier and $\mu_0 H_0$ is the critical field for reversal, at T=0 K. Then, considering that during the measurement time only energy barriers up to about 20-25 $k_B T$ are accessible, that is $E \approx$ 20-25 k_BT, the coercive field may be expressed as:

$$\mu_0 H_C = \mu_0 H_0 - \left[\frac{\mu_0 H_0 25\ k_B}{E_0}\right] T\ . \tag{2}$$

The estimated values of $\mu_0 H_0$ and $E_{0,}$ obtained by fitting the experimental data to eq. 2, are listed in Table 4.

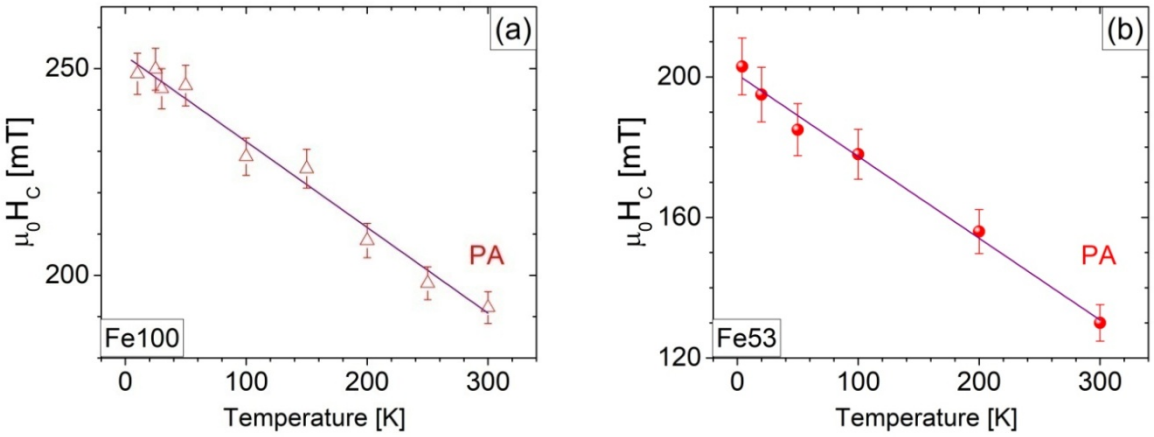

Figure 6. Temperature dependence of coercivity in (a) Fe100 and (b) Fe53 arrays, corresponding to PA configuration. Solid lines are the best linear fits to eq. 2.

Table 4. Coercive field at T = 0 K, $\mu_0 H_0$, and the activation energy at zero applied field, E_0 corresponding to the PA configuration. Activation energy E_0 results from the best fit of eq. 2 to data.

Sample	$\mu_0 H_0$ [mT]	E_0	
		[kJ/mol]	[eV]
Fe100	253±4	250±10	2.6±0.1
Fe53	201±2	180±20	1.8±0.1

The activation energy value for Fe53 is smaller but of the same order of magnitude than the ones reported by Paulus et al. [28] for the nucleation of inverse domains in large-grained Fe NWs (2.4 - 5.1 eV). This reduced activation barrier is likely to arise from the smaller grain size of the synthesized samples, with a larger density of disordered zones, such as grain boundaries. The activation energy barrier is larger in Fe100 NWs than in the bimetallic and biphasic Fe53 ones, which is consistent with the large shape anisotropy $K_{sh} (= \frac{1}{4\mu_0} J_S^2 \cong 920$ kJ/m^3) in iron NWs. Besides, these NWs have a very large grain size (~ 100 nm) and relatively smooth surfaces with no visible branching (see Figure 1.e), so they are expected to contain a lower density of efficient sites acting as catalysts for inverse domain nucleation.

In biphasic NWs, the domain wall energy density is larger in sites of the $L1_0$-FeNi ordered phase due to its large magnetocrystalline energy of about 700 kJ/m^3, two orders of magnitude larger than that of A1-FeNi (1.1 kJ/m^3).

Then, inverse domains are likely to nucleate in the soft A1-FeNi phase. However, this soft phase is exchange-coupled to the harder one, and a higher effective anisotropy value is expected. Another factor reducing the zero field activation barriers is the magnitude of local stray fields, and atomic defects which are both more important at the nucleation sites near interfaces.

As a linear relationship between coercive field and temperature is consistent with different magnetization reversal mechanisms, such as weak domain wall pinning and localized nucleation of inverse domains [29], additional measurements have to be considered to confirm that nucleation of inverse domains is actually the responsible mechanism for the observed coercivity. The coercive field dependence on the angle ϕ between the applied magnetic field and the NWs long axis (easy magnetization axis) is closely related to the operating reversal mechanism, so this aspect is further investigated at room temperature in both samples Fe100 and Fe53.

The magnetization reversal mechanism controlling coercivity in polycrystalline Fe nanowires has been reported to be the nucleation of inverse domains by local curling and the further expansion of these regions to the entire grain [30]. The angular dependence of the nucleation field in a small prolate spheroid (nucleus) with an effective uniaxial anisotropy K_U, given by contributions of crystalline and shape anisotropies, is described by [30, 31]:

$$\mu_0 H_C(\phi) = \mu_0 \frac{2 K_u}{J_s} \frac{(n_{\parallel} - s)(n_{\perp} - s)}{\sqrt{(n_{\parallel} - s)^2 \sin^2\phi + (n_{\perp} - s)^2 \cos^2\phi}} - N_{eff} J_S, \quad (3)$$

with $s = \frac{4k L_x^2}{D^2}$ taking values of 0.0482 and 0.0583 for Fe100 and Fe53 arrays, respectively; k = 1.2049 [32]; A is the exchange energy constant, and $L_x = \sqrt{\frac{2A\mu_0}{J_S^2}}$ the exchange length, being composition sensitive through J_S. The parameters $n_{\parallel}$ and $n_{\perp} = (1 - n_{\parallel})/2$ represent the nucleus effective demagnetizing factors. A mean value of the dipolar interaction field for angles $0 < \phi < \pi/2$ is included as a second term in the right hand side of eq. 3.

Figure 7 depicts the angular variation of the coercive field for array Fe53. The solid line in Figure 7.b corresponds to the best fit of eq. 3 to the data displayed in Figure 7.a; the resulting parameters' values are listed in Table 5.

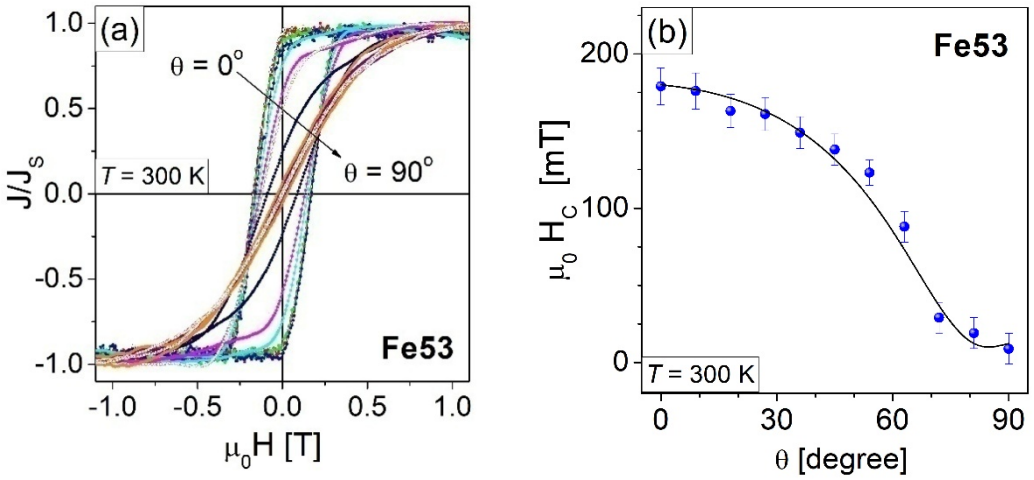

Figure 7. (a) Angular dependence of the hysteresis loop of array Fe53. (b) Coercive field as a function of the angle between the applied magnetic field and the NWs long axis. The solid line is the best fit of eq. 3 to the experimental data; values of the main fitted parameters are displayed in Table 5.

Table 5. The effective uniaxial anisotropy K_u and the effective demagnetizing factor N_{eff} are given together with values of the shape anisotropy K_{sh} and the magnetocrystalline one K_1, at room temperature.

Sample	K_u [kJ/m^3]	K_{sh} [kJ/m^3]	K_1 [kJ/m^3]	N_{eff}
Fe100†	820	920	48	0.07
Fe53	130	560[a] 370[b]	700[a] 1[b]	0.20

† Data for pure Fe NWs are taken from ref. [33]. [a] $L1_0$-FeNi; [b] A1-FeNi.

The effective uniaxial anisotropy constant K_U is larger in the Fe100 array than in Fe53, indicating that the uniaxial effective anisotropy is controlled by the shape contribution. In fact, K_{sh} and K_U take quite similar values in iron samples

In the case of sample Fe53, the scenario is more complex. Larger global and local magnetostatic effects are present in these bi-metallic nanowires. A relatively low value of effective uniaxial anisotropy K_U is observed, as compared to the upper bounds for shape anisotropy K_{sh} calculated for single phase A1-FeNi NWs and $L1_0$-FeNi NWs, listed in Table 5. Such a low value of K_U may be expected for granular and biphasic NWs which in addition are not perfect cylinders. In fact, large *local* stray fields at the external surface defects, as well as at internal boundaries between phases with different saturation polarization affect local nucleation conditions, becoming more important than the shape anisotropy values estimated assuming a perfect cylindrical geometry, with a large aspect ratio. Also due to the internal stray fields, the apparent demagnetizing factor N_{eff} is larger in sample Fe53. Then, irregular morphologies and rough surfaces do not change the nucleation/expansion magnetization reversal mechanism acting in polycrystalline cylindrical nanowires, but they offer many nucleation sites with lower activation barriers leading to also lower coercivity.

On the other hand, the effective uniaxial anisotropy K_U = 130 kJ/m^3 obtained is larger than the magnetocrystalline anisotropy of the disordered phase, reaching the order of magnitude reported for the hard ordered phase. This experimental value is quite close to the effective one of 170 kJ/m^3 estimated from the blocking temperature in the first part of this section. Then, it may be concluded that there exists a strong exchange coupling between hard and soft phases which modify the effective uniaxial anisotropy at the nucleation sites in the soft grains, preferably located near defects and interfaces.

4. Conclusion

Granular Fe-Ni nanowire arrays with nominal composition Fe_xNi_{100-x} (x = 0, 18, 53, 93, 100) have been synthesized by AC electrodeposition into the cylindrical pores of an alumina template. Except for the composition $Fe_{53}Ni_{47}$, NWs are single phase, consisting of small grains of the A1-FeNi disordered phase. Near the equiatomic nominal composition NWs are biphasic, consisting of grains of the A1-FeNi disordered phase (γ-FeNi phase) and grains of the $L1_0$-FeNi ordered phase (γ''-FeNi phase). These phases, with quite different magnetocrystalline energies, (the one for γ''-FeNi phase is 700 times larger than that corresponding to the γ-FeNi phase), are present in the NWs with similar grain sizes. These NWs display a single magnetic phase, as no different switching fields may be resolved for each phase, indicating that they are exchange-coupled in the temperature range between 5 K and 300 K. The exchange-hardening of the soft A1-FeNi disordered (γ-FeNi) phase leads to larger coercive fields near the equiatomic

composition, as compared to that observed in single-phase A1-Fe-Ni NWs, in which coercivity is governed by shape anisotropy.

The polarization reversal mechanism in the biphasic NWs array is found to be the nucleation and expansion of inverse domains, assisted by thermal fluctuations and the applied field. This mechanism is consistent with the linear dependence of the coercive field on temperature in the range 5 K - 300 K and the dependence of this coercive field on the angle between the NWs long axis and the applied field. The angular dependence of the coercive field may also be well described by considering a localized nucleation mode, in which inverse domains (nuclei) form by curling. The effective uniaxial anisotropy resulting from these measurements is in good agreement with a little influence of the global shape anisotropy and nucleation events at favorable sites in the exchange-hardened γ-FeNi soft phase.

Acknowledgements

The authors thank SECyT-UNC, Foncyt and CONICET Argentina for the financial support given to this work.

References

[1] Robert O'Handley, *Modern magnetic materials: Principles and Applications,* 2000, John Wiley & Sons Inc., New York, pp.367.

[2] S. Goolaup, M. Ramu, C. Murapaka, W. S. Lew. "Transverse domain wall profile for spin logic applications". Sci. Rep. **5** (2015) 9603.

[3] V. Raj Shrestha, S. S. Lee, E. S. Kim, D. Y. Choi. "Polarization-tuned dynamic color filters incorporating a dielectric-loaded aluminum nanowire array". Sci. Rep. **5** (2015) 12450.

[4] L. Vivas, et al. "Magnetic anisotropy in coni nanowire arrays: analytical calculations and experiments". Phys. Rev. B **85** (2012) 035439.

[5] Q. Liu, J. Wang, Z. Yan, D. Xue."Characterization and magnetic properties of Fe(1-x) Ni(x) nanowire arrays". Phys. Rev. B **72** (2005) 144412.

[6] T. M. Nguyen, M. G. Cottam. "Coupled dipole-exchange spin waves in arrays of interacting ferromagnetic nanowires". J. Mag. Magn. Mater. **310** (2007) 2433–2435.

[7] G. Béranger, F. Duffault, J. Morlet, J.-F. Tiers. *Les Alliages de Fer et de Nickel. Cent ans apres la découverte de l'Invar.* Londons–Paris–New York: Lavoisier–Technique & Documentation. 1996.

[8] M. Almasi Kashi, A. Ramazani, S. Doudafkan, A. S. Esmaeily. "Microstructure and magnetic properties in arrays of ac electrodeposited Fe(x)Ni(1−x) nanowires induced by the continuous and pulse electrodeposition". Appl. Phys. A 102 (2011) 761–764.

[9] A. Ramazani, V. Asgari, A.H. Montazer, M. A. Kashi. "Tuning magnetic fingerprints of FeNi nanowire arrays by varying length and diameter". Curr. Appl. Phys. Vol.15, **7** (2015) 819-828.

[10] T. B. Massalski, editor. Binary alloy phase diagrams. Materials Park (OH): ASM; 1986.; R. A. Howald. Metall. Mater. Trans A 34 (2003) 1759.

[11] K. B. Reuter, D. B. Williams, J. I. Goldstein. "Determination of the Fe-Ni Phase Diagram below 400 °C". Metall. Trans. A **20** (1989) 719-725.

[12] C. W. Yang, D. B. Williams, J. I. Goldstein. "A revision of the Fe-Ni phase diagram at low temperatures (<400 °C)". J Phase Equilib. 17 (1996) 522-531.

[13] H. Masuda, K. S. Fukuda. **"**Ordered Metal Nanohole Arrays Made by a Two-Step Replication of Honeycomb Structures of Anodic Alumina". Science **268** (1995) 1466-1468.

[14] Xiuli Zhang, Huimin Zhang, Tianshan Wua ZiyueLi, Zhijun Zhang, Huiyuan Sun. "Comparative study in fabrication and magnetic properties of FeNi alloy nanowires and nanotubes". J. Mag. Magn. Mater. **331** (2013) 162–167.

[15] Xiaoming Kou, Xin Fan, R. K. Dumas, Qi Lu, Yaping Zhang, Hao Zhu, Xiaokai Zhang, Kai Liu, J. Q. Xiao. "Memory Effect in Magnetic Nanowire Arrays". Adv. Mater. **23 (**2011) 1393–1397.

[16] D. Al Mawlawi, N. Coombs, M. Moskovits, "Magnetic properties of Fe deposited into anodic alumina oxide pore as a function of particle size", J. Appl. Phys. **70** (1991) 4421-4425.

[17] D. J. Sellmyer, M. Zheng, R. Skomski, "Magnetism of Fe, Co and Ni nanowires in self-assembled arrays", J. Phys.: Conden. Matter **13** (2001) R433-R460.

[18] K. Nielsh, J. Choi, K. Schwirn, R. B. Wehrspohn, U. Gosele."Self-ordering Regimes of Porous Alumina: The 10% Porosity Rule". Nano Lett. **2** (2002) 677–680.

[19] J. Bandyopadhyay, K. P. Gupta, "Low temperature lattice parameter of nickel and some nickel-cobalt alloys and Grfineisen parameter of nickel Lattice". Cryogenics (1977) 345-347.

[20] Y. Mishin, M.J. Mehl, D.A. Papaconstantopoulos. "Phase stability in the Fe–Ni system: Investigation by first-principles calculations and atomistic simulations". Acta Materialia **53** (2005) 4029–4041.

[21] M. Kotsugi, H. Maruyama, N. Ishimatsu, N. Kawamura, M. Suzuki, M. Mizumaki, K. Osaka, T. Matsumoto, T. Ohkochi, T. Ohtsuki, T. Kojima, M. Mizuguchi, K. Takanashi, Y. Watanabe. "Structural, magnetic and electronic state characterization of $L1_0$-type ordered FeNi alloy extracted from a natural meteorite". J. Phys.: Condens. Matter **26** (2014) 064206 -064218.

[22] T. Kojima, M. Ogiwara, M. Mizuguchi, M. Kotsugi, T. Koganezawa, T. Ohtsuki, T. Tashiro, K. Takanashi. "Fe–Ni composition dependence of magnetic anisotropy in artificially fabricated L10-ordered FeNi films". J. Phys.: Condens. Matter **26** (2014) 064207 (10pp).

[23] R. C. O'Handley. *Modern magnetic materials: principles and applications,* John Wyley & Sons, Inc. New York, p. 40 (2000).

[24] M. Knobel, W. C. Nunes, L. M. Socolovsky, E. De Biasi, J. M. Vargas, J. C. Denardin. "Superparamagnetism and other magnetic features in granular materials: a review on ideal and real systems". J. Nanosci. Nanotechnol. **8** (2008) 2836-2857.

[25] I. J. Bruvera, P. Mendoza Zélis, M. Pilar Calatayud, G. F. Goya, F. H. Sánchez. "Determination of the blocking temperature of magnetic nanoparticles: The good, the bad, and the ugly". J. Appl. Phys. **118** (2015) 184304.

[26] H. Kagawa, S. Chikazumi. "Anomalous magnetic anisotropy of Fe-Ni alloys". J. Phys. Soc. Japan, **48** (5) (1980) 1476-1481.

[27] S. Chikazumi. "Mechanism of high coercivity in rare-earth permanent magnets". J. Mag. Magn. Mater. **551** (1986) 54-57.

[28] P. M. Paulus, F. Luis, M. Kröll, G. Schmid, L. J. de Jongh. "Low-temperature study of the mgnetization reversal and magnetic anisotropy of Fe, Ni, and Co nanowires". J. Magn. Mag. Mater. **224** (2001) 180-196.

[29] P. Gaunt. "Magnetic viscosity and thermal activation energy". J. Appl. Phys. **59** (1986) 4129.

[30] M. S. Viqueira, N. Bajales, S. E. Urreta, P. G. Bercoff. "Magnetization mechanisms in ordered arrays of polycrystalline $Fe_{100-x}Co_x$ nanowires". J. Appl. Phys. **117** (2015) 204302.

[31] A. Aharoni. "Angular dependence of nucleation by curling in a prolate spheroid". J. Appl. Phys. **82** (1997) 1281.

[32] A. Aharoni, S. Shtrikman. "Magnetization Curve of the Infinite Cylinder". Phys. Rev. **109** (1958) 1522.

[33] J. S. Riva, G. Pozo-López, A. M. Condó, M. S. Viqueira, S. E. Urreta, D. R. Cornejo, L. M. Fabietti. "Biphasic FeRh nanowires synthesized by AC electrodeposition". J. All. Comp. **688** (2016) 804-813.